Research Square

Preprints are preliminary reports that have not undergone peer review.
They should not be considered conclusive, used to inform clinical practice,
or referenced by the media as validated information.

Synergistic Microbiologically Influenced Corrosion of SLM TC4 by Co-culture of Streptococcus mutans and Veillonella dispar via Riboflavin-Mediated Extracellular Electron Transfer

yilan wang
Hangzhou Medical College
kuiwei zheng
Hangzhou Medical College
zhenyu liu
Zhejiang Provincial People's Hospital
hongxiang yuan
The First People's Hospital of Lin 'an
xiaohua fu
Zhejiang Provincial People's Hospital
xing zhou
zhouxing2023@hmc.edu.cn

Hangzhou Medical College

Article

Keywords: Dental implants, Microbiologically influenced corrosion, Streptococcus mutans, Veillonella dispar, Extracellular electron transfer

Posted Date: June 30th, 2026

DOI: https://doi.org/10.21203/rs.3.rs-10050682/v1

License: This work is licensed under a Creative Commons Attribution 4.0 International License.
Read Full License

Additional Declarations: No competing interests reported.

Version of Record: A version of this preprint was published at npj Materials Degradation on October 5th, 2026. See the published version at https://doi.org/10.1038/s41529-026-00892-8.

Abstract

Ti-6Al-4V (TC4) is extensively utilized for oral implants due to its excellent mechanical properties and biocompatibility. In the oral environment, microbiologically influenced corrosion (MIC) is typically driven by multispecies biofilms. Here, electrochemical, surface, and corrosion product analyses were used to investigate the MIC of selective laser melted (SLM) TC4 induced by mono- or dual-species biofilms of *Streptococcus mutans* (*S. mutans*) and *Veillonella dispar* (*V. dispar*). The dual-species biofilm was thicker, denser, and produced more extracellular polymeric substances (EPS) than mono-species biofilms, resulting in higher corrosion current density and lower charge transfer resistance. Although *S. mutans* dominated the interaction, *V. dispar* alone accelerated corrosion mainly via extracellular electron transfer (EET), as confirmed by riboflavin addition. The co-culture system's overall pH increased, ruling out acid-induced corrosion as the main mechanism. Instead, their synergy promoted EET-MIC, further enhanced by riboflavin as an electron shuttle. Corrosion product analysis showed that under dual-species conditions, TiO_2 in the passive film decreased significantly, while Ti, Al, and V ion release increased, indicating lower corrosion resistance. Cytotoxicity and cytoskeletal staining revealed that the dual-species biofilm corrosion solution more strongly stimulated cell growth and proliferation. Our findings offer new insights into oral MIC mechanisms and strategies for developing corrosion-resistant oral materials.

1. Introduction

Dental implants are widely adopted for tooth loss restoration and aesthetic reconstruction. TC4 exhibits excellent mechanical properties, biocompatibility, corrosion resistance, and a low elastic modulus, rendering it a standard material for dental implant fabrication [1]. Compared to traditional manufacturing, which suffers from complex procedures and material waste, SLM, as an additive manufacturing technology, enables the direct fabrication of dental implants with customized morphology, good mechanical strength, and biocompatibility [2–6]. Modern medicine has made great progress in surgical implant restoration. However, postoperative implant infection remains a key factor causing failure in oral and orthopedic implant therapy [7]. Reports show that the incidence of peri-implantitis is 22%-43% in different patient groups 5–10 years after implantation [8,9]. The warm, moist, and nutrient-rich oral environment has aerobic, microaerophilic, and anaerobic microenvironments, which support the growth of corrosive microorganisms [10]. Biofilms with diverse microorganisms colonize oral surfaces (oral epithelium, gingival sulcus, tongue, soft and hard palate, tooth surfaces) and dental devices (restorations, dentures, orthodontic brackets, archwires) [11]. These biofilms consist of EPS, microorganisms, and their metabolites, leading to localized changes in pH, dissolved oxygen levels, ion concentrations, and organic content [12]. These factors together accelerate the corrosion and degradation of dental metallic materials, producing toxic byproducts and releasing metal ions [13]. This further disrupts cellular metabolism and proliferation, causing local tissue edema, infection, and even necrosis, and may lead to systemic adverse reactions, which is a critical clinical challenge [14].

MIC is a biofilm-mediated bioelectrochemical process that occurs in nearly all environments containing microorganisms, including marine settings, oil-water interfaces, soil, medical implants, and even space stations [15–17]. Biofilms are the main cause of degradation of various metals and alloys [18]. Microorganisms in biofilms induce or accelerate corrosion through two main mechanisms: Metabolite-MIC (M-MIC), caused by microbial corrosive byproducts like organic acids, and Extracellular Electron Transfer-MIC (EET-MIC), from electroactive microorganisms extracting electrons from metals [19,20]. Previous studies investigated the effects of single strains (*S. mutans*, *Actinobacillus*, *Candida albicans*, *Porphyromonas gingivalis*, *Streptococcus sobrinus type g*) on corrosion, surface tarnish, discoloration, and microbial adhesion of traditional-process oral metals (pure Ti, Ti75 alloy, 316L stainless steel, cobalt-chromium alloy, nickel-chromium alloy) [21–24]. However, in-situ oral biofilms are symbiotic, synergistic multi-species communities, with physicochemical properties and corrosion behaviors significantly different from single-strain biofilms. Current single-strain-based research on metabolism-mediated microbial corrosion cannot fully reflect the actual corrosion kinetics of implant metals, often leading to limited and one-sided interpretation of corrosion mechanisms [25]. Additionally, due to limited prior discussion on electroactive oral biofilms, the possibility of EET-MIC occurring in the oral environment has been largely overlooked.

The oral cavity harbors a vast number of microorganisms, among which *S. mutans* is an early colonizer and a typical acid-producing bacterium [26]. The primary virulence factor of *S. mutans* is its ability to adhere to tooth surfaces and form polysaccharide-encapsulated biofilms, characterized by causing localized demineralization and decay of teeth [27]. Previous studies confirmed that *S. mutans* can produce acidic microenvironments through metabolic acid production, change implant surface morphology and chemical composition, and thus damage the surface oxide film of titanium-based implants [28]. Using 16S rRNA sequencing, Wang et al. identified multiple electroactive microorganisms (*Veillonella*, *Actinomyces*, *Staphylococcus*) in supragingival plaque samples from healthy volunteers [10]. Furthermore, *Veillonella* is abundant in implant infection-related biofilms, possibly due to its interactions with some oral bacteria [29,30]. Research suggests *V. dispar* forms a potential “criminal consortium” through interactions with *S. mutans* [31,32]. *Veillonella* promotes *Streptococcus* growth and its biofilm resistance, and *Streptococcus* provides it with adhesion sites and nutrients [33]. *V. dispar* has a weak adherence ability to tooth surfaces and requires co-aggregation with streptococci for initial colonization [34,35]. The two genera exhibit interdependent relationships in spatial distribution, adhesion, nutrient utilization, and interspecific signal communication [36]. Liu found that in dual-species biofilms, *Veillonella parvula* promoted *S. mutans* growth and extracellular polysaccharide synthesis [37].

Currently, research on the MIC of metallic dental implants mediated by symbiotic bacteria remains extremely limited, with no studies focused on additively manufactured implants. This study investigates the MIC of TC4 alloy by mixed bacterial communities of *V. dispar* and *S. mutans*, using single-strain controls for comparison. Through electrochemical testing, surface analysis, and characterization techniques, biofilm and corrosion products were examined. Cytotoxicity assays evaluated material

biosafety. This work provides an in-depth analysis of the mechanistic roles of these two bacterial strains in the MIC of TC4.

2. Materials and methods

2.1 Materials preparation

The SLM TC4 alloy employed in this study had the following nominal composition (wt. %): Ti 90.71, Al 5.51, V 3.78. The specimens were prepared as square blocks measuring 10 mm × 10 mm × 3 mm. Prior to testing, all samples were mechanically ground using successive grades of 400 #, 600 #, 800 #, 1000 #, and 1200 # SiC sandpapers to remove surface oxide layers and attain a uniform surface finish. Subsequently, specimens were ultrasonically cleaned in absolute ethanol and distilled water for 15 min each, and then sterilized by exposure to ultraviolet radiation for 30 min with the test surface oriented upwards. The specimens for electrochemical experiments were embedded in epoxy resin, exposing a 10 mm × 10 mm surface area for testing.

In this study, *V. dispar* (DSM 20735) and *S. mutans* (ATCC 25175) were utilized establish a biofilm consortium. *V. dispar* and *S. mutans* were cultured in 136 medium and BHI medium, respectively. The composition of the 136 medium consisted of: 5 g/L tryptone, 3 g/L yeast extract, 7.5 g/L Na-(DL)-lactate, 0.75 g/L sodium thioglycolate, 1 mL/L Tween 80, 1 g/L glucose, 0.003 g/L putrescine, and 0.001 g/L resazurin. All media were autoclaved at 121°C for 30 min, and the pH was adjusted to 7.5 ± 0.1 with potassium carbonate after cooling. Prior to use, the media were placed in an anaerobic chamber for 48 h to eliminate dissolved oxygen. All biocorrosion tests were conducted in an anaerobic chamber under a nitrogen atmosphere. The initial cell concentration was adjusted to 10^6 cells/mL. Electrochemical tests were performed in 500 mL glass cells containing 250 mL of medium under anaerobic conditions at 37°C for 14 days.

2.2 Biofilm and coupons surface morphologies

The viability and thickness of biofilms on the sample surfaces were assessed using a confocal laser scanning microscope (CLSM, C2 Plus, Nikon, Japan). Prior to CLSM observation, the samples were incubated in culture medium for 7 and 14 days. Subsequently, the biofilms were stained in the dark for 20 minutes with a fluorescent dye (BacLight Bacterial Viability Kit, Invitrogen, Thermo Fisher Scientific, USA), followed by rinsing with sterile water to remove unbound dye. The biofilm thickness was determined by scanning the three-dimensional images obtained via CLSM at an excitation wavelength of 483 nm and an emission wavelength of 503 nm.

Additionally, CLSM was utilized to evaluate the surface coverage of cells and EPS. Biofilm samples were prepared as described above. After 7 and 14 days of incubation, samples were collected from different experimental conditions, rinsed with sterile water to remove planktonic cells, and subsequently treated with 0.1% Triton X-100 solution for 30 min to permeabilize cell membranes. The samples were then incubated sequentially in the dark with undiluted DAPI (4,6-diamidino-2-phenylindole), Alexa 633-

conjugated concanavalin A, and SYPRO tangerine for 15 min each. All procedures were performed under dark conditions.

2.3 Corrosion pit morphology and surface corrosion product detection

Field emission scanning electron microscopy (FESEM, Ultra-Plus, Zeiss, Germany) was employed to examine the morphology of biofilms on the coupon surfaces. After immersion in the culture medium for 7 and 14 days, the samples were rinsed with phosphate-buffered saline (PBS) to remove loosely attached biofilms and planktonic cells, then fixed in 2.5% (v/v) glutaraldehyde solution for 4 h, followed by dehydration using a graded ethanol series. Prior to SEM observation, the coupons were sputter-coated with gold to enhance electrical conductivity.

The distribution and depth of corrosion pits were examined using laser scanning confocal microscopy (CLSM, LSM 710, Zeiss, Germany). After 14 days of immersion, the specimens were retrieved and subjected to the ASTM G1-03 standard chemical cleaning procedure to remove residual biofilms and corrosion products the pits.

The corrosion products after immersion were analyzed by X-ray photoelectron spectroscopy (XPS, ESCALAB 250, Thermo Fisher, MA, USA). Following 14 days of co-culturing, samples from the mono-species, dual-species, and sterile control groups were collected, rinsed with deionized water, dried, and prepared for XPS analysis. The XPS analysis was performed using a monochromatic Al Kα X-ray source (1486.6 eV) operated at 1500 eV. High-resolution spectra were acquired with a pass energy of 50 eV and an energy step size of 0.1 eV over a binding energy range of 0–1350 eV. All collected spectra were calibrated by referencing the C 1s peak at 284.8 eV for charge correction.

2.4 Electrochemical tests

To investigate the corrosion behavior of TC4 alloy induced by *S. mutans*, *V. dispar*, and their co-culture, electrochemical measurements were conducted over 14 days under anaerobic conditions at 37°C using an electrochemical workstation (Reference 600, Gamry Instruments, Inc., USA). A conventional three-electrode system was employed, with a saturated calomel electrode (SCE) as the reference electrode, a platinum sheet as the counter electrode, and the TC4 specimen as the working electrode. Open circuit potential (OCP), linear polarization resistance (LPR), electrochemical impedance spectroscopy (EIS), and potentiodynamic polarization tests were performed. After stabilization of the OCP, LPR measurements were carried out within a potential range of ± 10 mV vs. E_{OCP} at a scan rate of 0.125 mV/s. Subsequently, EIS was conducted over a frequency range of 10^5 Hz to 0.01 Hz with an AC voltage amplitude of 5 mV (vs. SCE). On day 14, potentiodynamic polarization tests were performed by scanning from − 500 mV to 1500 mV vs. E_{OCP} at a sweep rate of 0.166 mV/s. The corrosion current densities (i_{corr}) and corrosion potentials (E_{corr}) were obtained through Tafel extrapolation.

2.5 Analysis of dissolved metal ion concentrations and Cytotoxicity

Metallic ions released from coupons immersed in media containing mono-species, dual-species, and sterile control groups for 7 and 14 days were analyzed. The solutions were transferred to 50 mL tubes and vortexed for 1 min to ensure homogeneous distribution of metallic ions. Subsequently, the solutions were filtered through 0.22 μm sterile membranes to remove bacterial cells and impurities. Dissolved metal ions in the filtrate were quantitatively analyzed using flame atomic absorption spectroscopy (FAAS, Model Z-2000, Hitachi, Japan), with an instrumental detection limit of 1 μg/L. The measured metal ion concentrations were normalized to the specimen's surface area for comparative assessment.

L-929 cells (Cat No. FH0534) purchased from Shanghai Fuheng Biotechnology, were cultured in cell culture flasks until they reached over 80% confluence. The cells were then digested with 0.25% trypsin and counted using a cell counting plate. After 14 days of co-culture in the presence or absence of microbial groups, the extracts were filtered and sterilized using a 0.22 μm syringe filter. The filtrate was added to L-929 complete culture medium at a ratio of 1:10 to prepare a 10% stock solution. The sample pieces were placed in 24-well plates, and 5,000 cells were seeded into each well. According to ISO 10993-12 [38], the culture medium was added at an extraction ratio of 3 cm^2/mL and incubated at 37°C for 24 and 72 hours. Then, 10% CCK-8 working solution was added, and the plates were incubated in the dark for 1.5 hours. The supernatant was transferred to a 96-well plate, and the optical density (OD) value was measured at a wavelength of 450 nm. The cell relative growth rate (RGR) was calculated according to formula (1).

$$RGR(\%) = OD_2 / OD_1 \times 100\% \quad (1)$$

Where RGR is the cell proliferation rate, and OD_2 and OD_1 are the absorbance values of the experimental and control groups at 450 nm, respectively.

Three replicates were set up for each experiment, and the experiment was repeated three times. Additionally, two parallel samples per group were placed in 24-well plates, and 2 mL of 10% stock solution was added to each well. Each well was seeded with 5,000 cells. After 1 and 3 days of culture, the cells were fixed with 4% paraformaldehyde for 30 minutes, permeabilized with 0.5% Triton X-100 for 5 minutes, stained with rhodamine-phalloidin in the dark for 50 minutes, and counterstained with DAPI for 10 minutes. Cell adhesion morphology was observed using a fluorescence microscope (Ti-U, Nikon, Japan).

3. Results

3.1 Formation and structure of biofilms on TC4 coupon surfaces

After 7 and 14 days of co-culture with *V. dispar* and *S. mutans*, observations were made using CLSM. Three-dimensional CLSM images revealed significant differences in biofilm thickness and viability among the different biofilms. As shown in Fig. 1 (a, b), green, red, and yellow signals correspond to live cells, dead cells, and partially damaged/dead cells, respectively. On day 7 of cultivation, the measured biofilm thicknesses were: *V. dispar* 16.3 ± 1.2 μm, *S. mutans* 33.7 ± 2.3 μm, and the mixed-species 36.5 ± 2.3 μm. The results indicate that, compared to mono-species biofilms, the mixed-species biofilm was thicker, denser, and contained a higher number of sessile cells. Subsequently, due to cell apoptosis and nutrient depletion, the number of sessile cells in the biofilms decreased rapidly, accompanied by a corresponding increase in the proportion of dead cells. By day 14, the biofilm thickness measurements were: *V. dispar* 12.2 ± 2.6 μm, *S. mutans* 21.9 ± 1.1 μm, and the mixed-species 31.2 ± 4.1 μm

Under the same culture conditions, sequential staining techniques were employed to label cells, proteins, and polysaccharides on the sample surfaces, followed by evaluation using CLSM to assess the differences in cellular, protein, and polysaccharide composition among the different biofilms. Figure 1 (c, d) illustrates the biofilm architecture by merged fluorescence channels of cells (blue), proteins (red), and polysaccharides (green), indicating that these three components are widely distributed within the biofilm matrix. On day 7, the mixed-species biofilm exhibited higher cell density, protein concentration, and polysaccharide content compared to mono-species biofilms, suggesting increased biofilm thickness, elevated metabolite production, and enhanced EPS secretion on the metal surface. Figure 1 (d) shows that after 14 days of co-culture with the mixed species, the surface content of cells, proteins, and polysaccharides on the samples decreased compared to day 7, likely due to nutrient depletion leading to a reduction in bacterial EPS synthesis capacity. In this study, *V. dispar* exhibited relatively limited EPS production due to its inability to ferment sugars. *S. mutans* catalyzes glucosyl transfer through one or more glucosyltransferases (GTFs), which participate in the synthesis of extracellular polysaccharides by this organism [27]. Under mixed-species conditions, lactate consumption by *V. dispar* alleviates microenvironmental acidosis, thereby promoting EPS production by *S. mutans* and ultimately driving the formation of thicker biofilms [37]. Furthermore, consistent with the live/dead staining results, on day 7 of co-culture, *S. mutans* and *V. dispar* exhibited interbacterial co-aggregation, with the formation of extensive viscous EPS encapsulating the bacterial cells, thereby contributing to increased biofilm thickness. By day 14, the overall biofilm activity showed a declining trend, the structure became looser, and EPS coverage was significantly reduced in localized areas.

3.2 Morphology of biofilms and pitting observation

The adhesion morphologies of *V. dispar*, *S. mutans*, and the *V. dispar-S. mutans* co-culture on TC4 surfaces after 7 and 14 days of incubation are shown in Fig. 2 (a, b). After 7 days, *V. dispar* cells, predominantly existing as diplococci, were dispersed across the sample surface. The metal surface co-cultured with *S. mutans* for 7 days exhibited intermittent biofilms with round chains of sessile bacterial cells. In the dual-species culture, *S. mutans* initially adhered to the metal surface, followed by the attachment of *V. dispar* onto the pre-formed streptococcal layer, resulting in the development of mound-

shaped, synergistic biofilms with significantly increased microbial density and thickness. In contrast, the density of both mono- and dual-species biofilms had decreased after 14 days. These findings demonstrate that the biofilm architecture and adhesive capacity under mixed-species conditions differ markedly from those under mono-species conditions.

To evaluate the pitting corrosion, after removing corrosion products and biofilms, the morphology of TC4 specimens immersed for 14 days in sterile, single-species, and mixed dual-species culture media was observed using CLSM. The pitting depth and cross-sectional area under sterile, single-species, and mixed dual-species co-culture conditions were measured using CLSM. As shown in Fig. 2 (c-f), the maximum pit depths caused by *V. dispar*, *S. mutans*, and the *V. dispar-S. mutans* co-culture biofilms were 4.2 μm, 6.4 μm, and 9.4 μm, respectively. Samples soaked in sterile medium exhibited only the mildest irregular pitting, with an average depth of 1.4 ± 0.3 μm, whereas the average pit depths caused by *V. dispar*, *S. mutans*, and the mixed consortium biofilms were 3.1 ± 0.9 μm, 4.9 ± 2.2 μm, and 5.5 ± 1.5 μm, respectively. Compared with biofilms formed by a single strain, the presence of the mixed consortium led to more severe pitting corrosion on the TC4 samples.

3.3 Electrochemical measurements and Acid production by microbiota

3.3.1 OCP, corrosion rate versus time, and Potentiodynamic polarization curves

Figure 3 (a)illustrates the variation of open circuit potential (E_{OCP}) over time during a 14-day continuous culture for the sterile control group and the bacterial experimental group. In the sterile medium, the E_{OCP} of the TC4 specimen increased significantly from − 259 mV vs. SCE on the first day to − 175 mV by the third day, and then remained relatively stable thereafter, maintaining a level around − 160 mV. In contrast, in media containing *V. dispar* and *S. mutans*, the E_{OCP} exhibited a continuous negative shift during the first three days of incubation, reaching approximately − 499 mV and − 552 mV, respectively. Furthermore, in the medium containing the mixed dual-species consortium, the E_{OCP} values (approximately − 596 mV) were more negative than those observed under single-species conditions. The observed variations in E_{OCP} can be attributed to differences in the biofilm structures formed on the specimen surfaces [39].

As shown in Fig. 3 (b), LPR tests were conducted over a 14-day period in both sterile control and inoculated media to analyze corrosion rate variations under different conditions. Overall, the corrosion rates under all conditions fluctuated after one day of inoculation and subsequently stabilized at relatively constant values. Compared with the sterile medium (6.0 Ω·cm²), the lower polarization resistance (R_p) values observed in the presence of *V. dispar* (2.8 Ω·cm²) and *S. mutans* (2.3 Ω·cm²) indicate that both bacterial strains are corrosive. The lowest R_p value (1.7 Ω·cm²), detected in the mixed microbial consortium medium, suggests the existence of synergistic MIC. These results corroborate the conclusions drawn from the aforementioned surface analysis.

Figure 3 (c) displays the potentiodynamic polarization curves of TC4 specimens after 14-day exposure to sterile medium, *V. dispar*, *S. mutans*, and mixed consortium cultures. The corresponding electrochemical parameters extracted from the potentiodynamic polarization curves are presented in Fig. 3 (d). Compared with the sterile medium, the corrosion potentials shifted negatively in the presence of oral microbiota, which is consistent with the open-circuit potential monitoring results. The corrosion current density (i_{corr}) in the sterile medium (7.7 ± 1.0 nA·cm^{-2}) was significantly lower than that in the *V. dispar* inoculated medium (17.5 ± 1.2 nA·cm^{-2}), the *S. mutans* inoculated medium (24.2 ± 2.7 nA·cm^{-2}), and the mixed consortium inoculated medium (40.7 ± 2.0 nA·cm^{-2}). The corrosion potential and corrosion current density data (Fig. 3 (d)) further confirm that the mixed consortium biofilm induced a significantly higher corrosion rate compared to the single-species biofilms, which may be attributed to enhanced charge transfer between the TC4 surface and the mixed biofilm.

3.3.2 EIS measurements

Under stable OCP conditions, EIS tests were performed on samples incubated in abiotic and biotic media at days 1, 4, 7, 10, and 14. The corresponding Nyquist plots are presented in Fig. 4 (a-d), and the Bode plots (phase angle vs. log frequency) are shown in Fig. 4 (e-h). In general, the diameter of the capacitive arc in a Nyquist plot reflects the charge transfer resistance at the interface between the specimen and the electrolyte, a value that is negatively correlated with the material's corrosion susceptibility [40]. In the sterile medium (Fig. 4 (a)), the capacitive arc diameter was the largest and showed minimal variation over time. However, in media inoculated with *V. dispar* (Fig. 4 (b)) and *S. mutans* (Fig. 4 (c)), the observed incomplete capacitive arcs exhibited diameters smaller than those of the sterile group and continued to decrease with incubation time. Under the presence of mixed bacterial species, the capacitive arc diameter was the smallest, indicating the lowest corrosion resistance, which suggests that the corrosion rate in the presence of biofilms was significantly higher than that in the sterile control group.

The corresponding Bode plots (phase angle vs. logarithm of frequency) are shown in Fig. 4 (e-h). In the very high-frequency region, the impedance modulus represents the solution resistance. Based on the results, it can be inferred that the solution resistances of the four groups did not change significantly, indicating that the environmental conditions remained essentially consistent across groups during the immersion period. In the presence of microbes, both the maximum phase angle and the maximum phase angle amplitude were slightly reduced and narrowed. At low frequencies, a dual-phase film was formed on the alloy surface, consisting of an inner barrier layer and an outer porous layer. Therefore, the decrease in phase angle at low frequencies suggested a reduced contribution of surface film resistance to impedance [40]. The impedance modulus in the very low-frequency region represents the polarization resistance of the electrode. Significant differences in the low-frequency impedance modulus were observed among the four groups over time, suggesting that the structure of the passive layer under biofilm conditions differed markedly from that in the sterile medium.

The impedance spectra of specimens in different culture media were fitted using the equivalent electrical circuits (EEC) model illustrated in Fig. 4 (a-d). The impedance spectra under both sterile and bacteria-containing conditions showed good agreement with the circuit model. The equivalent circuit parameters obtained from electrochemical impedance spectroscopy measurements are listed in Table 1. Here, R_s represents the solution resistance, R_b denotes the resistance of the passive layer on the metal specimen, and R_{ct} stands for the charge transfer resistance. R_{ct} is an important parameter for the evaluation of MIC, which is inversely proportional to the corrosion rate [41]. Under all conditions, the passive layer resistance fluctuated over time and was significantly lower than the charge transfer resistance. According to the quantitative fitting data in Table 1, the R_{ct} of the mixed consortium on day 7 was only $4.5 \times 10^4 \pm 1.1 \times 10^4$ Ω·cm², which is one order of magnitude lower than that of the *V. dispar* monoculture group ($3.1 \times 10^5 \pm 8.0 \times 10^4$ Ω·cm^2) and the *S. mutans* monoculture group ($2.6 \times 10^5 \pm 4.7 \times 10^6$ Ω·cm^2), suggesting that the mixed bacterial community exhibits stronger corrosivity. The highest R_{ct} values were obtained in the abiotic medium, implying the excellent corrosion resistance of TC4 in the absence of biofilms. Under the condition of *V. dispar*, the R_{ct} values increased to $4.2 \times 10^5 \pm 3.6 \times 10^4$Ω·cm^2 on day 14. In the presence of *S. mutans*, the R_{ct} values decreased to $1.7 \times 10^5 \pm 4.5 \times 10^6$ Ω·cm² on day 14. In the mixed-species culture medium, the R_{ct} values on day 14 were ($1.0 \times 10^4 \pm 2.5 \times 10^5$) Ω·cm^2, which remained lower than those in both monoculture groups.

Table 1
EIS parameters extracted from EIS measurements during 14 days of incubation.

Duration/day	R_s	Q_f	R_b	Q_{dl}	R_{ct}
	(Ω cm^2)	(F cm^{-2})	(Ω cm^2)	(F cm^{-2})	(Ω cm^2)
TC4 in the sterile medium					
1	29.0 ± 0.8	$3.3 \times 10^{-5} \pm 4.0 \times 10^{-6}$	-	-	$9.6 \times 10^5 \pm 1.1 \times 10^5$
4	24.4 ± 0.7	$3.5 \times 10^{-5} \pm 6.0 \times 10^{-6}$	-	-	$3.1 \times 10^6 \pm 8.7 \times 10^7$
7	33.0 ± 2.5	$3.4 \times 10^{-5} \pm 2.1 \times 10^{-6}$	-	-	$3.8 \times 10^6 \pm 4.0 \times 10^7$
10	23.3 ± 0.9	$3.4 \times 10^{-5} \pm 4.0 \times 10^{-6}$	-	-	$5.8 \times 10^6 \pm 5.5 \times 10^7$
14	28.2 ± 0.8	$2.1 \times 10^{-5} \pm 4.9 \times 10^{-6}$	-	-	$2.3 \times 10^6 \pm 4.5 \times 10^7$
TC4 in the presence of *V. dispar*					
1	13.4 ± 0.7	$1.5 \times 10^{-5} \pm 3.5 \times 10^{-6}$	43.4 ± 0.5	$1.3 \times 10^{-5} \pm 5.8 \times 10^{-7}$	$5.3 \times 10^5 \pm 1.4 \times 10^5$
4	26.3 ± 0.9	$2.5 \times 10^{-5} \pm 2.5 \times 10^{-6}$	37.3 ± 0.8	$3.4 \times 10^{-5} \pm 2.0 \times 10^{-6}$	$4.9 \times 10^5 \pm 6.7 \times 10^4$
7	28.4 ± 0.5	$2.9 \times 10^{-5} \pm 1.7 \times 10^{-6}$	40.6 ± 1.6	$1.7 \times 10^{-5} \pm 4.0 \times 10^{-6}$	$3.1 \times 10^5 \pm 8.0 \times 10^4$
10	24.0 ± 0.8	$3.9 \times 10^{-5} \pm 3.1 \times 10^{-6}$	45.3 ± 0.9	$1.6 \times 10^{-5} \pm 2.6 \times 10^{-6}$	$3.2 \times 10^5 \pm 2.7 \times 10^4$
14	24.2 ± 0.7	$2.9 \times 10^{-5} \pm 7.6 \times 10^{-6}$	77.2 ± 1.2	$2.4 \times 10^{-5} \pm 8.7 \times 10^{-6}$	$4.2 \times 10^5 \pm 3.6 \times 10^4$
TC4 in the presence of *S. mutans*					
1	24.2 ± 0.8	$8.3 \times 10^{-5} \pm 3.7 \times 10^{-6}$	30.5 ± 1.4	$4.4 \times 10^{-5} \pm 1.0 \times 10^{-6}$	$4.7 \times 10^5 \pm 8.3 \times 10^4$
4	23.1 ± 0.9	$5.7 \times 10^{-5} \pm 6.0 \times 10^{-6}$	30.4 ± 1.4	$4.6 \times 10^{-5} \pm 6.0 \times 10^{-6}$	$2.7 \times 10^5 \pm 4.0 \times 10^6$

Duration/day	R_s	Q_f	R_b	Q_{dl}	R_{ct}
	(Ω cm^2)	(F cm^{-2})	(Ω cm^2)	(F cm^{-2})	(Ω cm^2)
7	29.0 ± 2.2	$3.3 \times 10^{-5} \pm 8.6 \times 10^{-5}$	29.5 ± 0.5	$3.7 \times 10^{-5} \pm 3.2 \times 10^{-6}$	$2.6 \times 10^5 \pm 4.7 \times 10^6$
10	30.4 ± 0.6	$3.2 \times 10^{-5} \pm 4.8 \times 10^{-6}$	31.3 ± 0.5	$1.4 \times 10^{-5} \pm 2.6 \times 10^{-6}$	$2.2 \times 10^5 \pm 3.2 \times 10^4$
14	10.0 ± 0.8	$9.1 \times 10^{-5} \pm 8.7 \times 10^{-6}$	19.4 ± 0.6	$2.6 \times 10^{-5} \pm 3.5 \times 10^{-6}$	$1.7 \times 10^5 \pm 4.5 \times 10^6$
TC4 in the presence of *V. dispar* + *S. mutans*					
1	24.8 ± 0.9	$2.2 \times 10^{-5} \pm 6.4 \times 10^{-6}$	8.9 ± 1.0	$4.7 \times 10^{-5} \pm 5.0 \times 10^{-6}$	$8.3 \times 10^4 \pm 1.2 \times 10^4$
4	25.6 ± 0.8	$3.7 \times 10^{-5} \pm 6.1 \times 10^{-6}$	13.2 ± 0.6	$1.9 \times 10^{-5} \pm 7.9 \times 10^{-6}$	$7.6 \times 10^4 \pm 6.5 \times 10^5$
7	10.1 ± 0.8	$2.1 \times 10^{-5} \pm 7.2 \times 10^{-6}$	14.5 ± 2.1	$4.5 \times 10^{-5} \pm 3.1 \times 10^{-6}$	$4.5 \times 10^4 \pm 1.1 \times 10^4$
10	33.1 ± 0.9	$3.1 \times 10^{-5} \pm 5.3 \times 10^{-6}$	11.4 ± 1.3	$1.9 \times 10^{-5} \pm 2.0 \times 10^{-6}$	$0.7 \times 10^4 \pm 1.4 \times 10^5$
14	24.2 ± 0.8	$5.7 \times 10^{-5} \pm 6.0 \times 10^{-6}$	7.4 ± 1.5	$2.5 \times 10^{-5} \pm 8.0 \times 10^{-6}$	$1.0 \times 10^4 \pm 2.5 \times 10^5$

3.3.3 Riboflavin concentration and pH measurements

To further investigate the fermentation behavior of *S. mutans* and *V. dispar* under co-culture conditions in the presence of titanium (Ti) alloy specimens, this study monitored the dynamic changes in the pH of the culture medium over 14 days, using sterile medium as a control. As shown in Fig. 5 (a), the pH in the abiotic medium exhibited minor fluctuations over time. In the medium inoculated with *S. mutans*, the pH decreased significantly to 5.7 on the first day and remained relatively stable thereafter. In the media inoculated with *V. dispar* and the dual-species consortium, the pH decreased to 6.4 and 6.3, respectively, on the first day, with no significant difference observed between the two.

Microbial communities can achieve more efficient utilization of energy from surrounding substances and better adapt to their living environment through electron exchange functions, a process that can also lead to increased corrosion. Riboflavin serves as an electron shuttle in the extracellular electron transfer process of various microorganisms [42]. In microbial fuel cells, riboflavin enhances current output by improving the efficiency of extracellular electron transfer. To validate this hypothesis, riboflavin at a final concentration of 10 μg/mL was added to the *V. dispar* culture medium. As shown in Fig. 5 (b), riboflavin

itself exhibited no corrosive effect under abiotic control conditions. On day 7, the R_{ct} of the *V. dispar* + 10 μg/mL riboflavin group was $2.1 \times 10^5 \pm 4.4 \times 10^4$ Ω·cm², lower than that of the *V. dispar* alone group ($3.1 \times 10^5 \pm 8.0 \times 10^4$ Ω·cm²). After 7 days, the difference in charge transfer resistance between the groups with and without riboflavin gradually diminished, although the final R_{ct} value in the riboflavin-supplemented group remained slightly lower. Potentiodynamic polarization curves and corresponding electrochemical parameters obtained on day 14 Fig. 5 (c, d) further corroborated the EIS data, indicating that riboflavin addition accelerated both the anodic reaction and corrosion rate of *V. dispar*-induced microbiologically influenced corrosion.

3.4 XPS analysis of passive film

To gain deeper insight into the corrosion products formed on TC4 surfaces under mono-species, dual-species, and sterile conditions, high-resolution XPS spectra of the Ti 2p, Al 2p, and V 2p regions were analyzed after 14 days of co-culture. The XPS survey scans (Table 2) detected Ti and O elements under all conditions, indicating that the passive film was primarily composed of titanium oxides. Further narrow-scan analysis of the Ti region identified specific titanium oxide species, and the relative percentages of these oxides were calculated based on the integrated peak areas [43]. Quantitative analysis of the Ti 2p spectra after etching to 3 nm, 7 nm, and 10 nm depths is shown in Fig. 6. In the sterile control, the proportion of Ti metal oxides was significantly higher than that of the metallic phase. The relative content of TiO_2 in the passive film plays a decisive role in the corrosion resistance of Ti alloys [30]. A higher proportion of TiO_2 corresponds to improved passive film stability and enhanced corrosion resistance [44]. In the presence of *V. dispar*, *S. mutans*, and their co-culture, the relative content of TiO_2 in the passive film was significantly lower. It can be concluded that both *S. mutans* and *V. dispar*, individually and in combination, accelerate the corrosion process by degrading the passive film, specifically through the reduction of TiO_2 content.

Table 2
Main compositions of the passive film at each XPS recording depth after 14 days of immersion under abiotic and biotic conditions

	Composition	Ti	Al	V
Sterile medium	0 nm	TiO_2	Al_2O_3	/
	3 nm	$TiO_2/Ti_2O_3/TiO$	Al_2O_3/Al	/
	7 nm	TiO/Ti^0	Al	V
	10 nm	Ti^0	Al	V
	18 nm	Ti^0	Al	V
V. dispar	0 nm	TiO_2	Al_2O_3	/
	3 nm	$TiO_2/Ti_2O_3/TiO$	Al_2O_3	/
	7 nm	$TiO_2/Ti_2O_3/TiO/Ti^0$	Al_2O_3/Al	V/V_2O_5
	10 nm	TiO/Ti^0	Al	V
	18 nm	Ti^0	Al	V
S. mutans	0 nm	TiO_2	Al_2O_3	/
	3 nm	$TiO_2/Ti_2O_3/TiO$	Al_2O_3	/
	7 nm	$TiO_2/Ti_2O_3/TiO/Ti^0$	Al_2O_3/Al	V/V_2O_5
	10 nm	TiO/Ti^0	Al	V
	18 nm	Ti^0	Al	V
V. dispar + *S. mutans*	0 nm	TiO_2	Al_2O_3	/
	3 nm	$TiO_2/Ti_2O_3/TiO$	Al_2O_3	/
	7 nm	$TiO_2/Ti_2O_3/TiO/Ti^0$	Al_2O_3/Al	V/V_2O_5
	10 nm	TiO/Ti^0	Al_2O_3/Al	V/V_2O_5
	18 nm	Ti^0	Al	V

3.5 Metal ions release and Cytotoxicity

In eukaryotic cells, an intricate fiber network called the cytoskeleton can reflect morphological changes of the cell [45]. According to different diameters, these fibers can be categorized into microfilaments, microtubules, and intermediate filaments. After staining the nucleus and cytoplasm with two dyes, the cytoskeleton morphology was examined under a fluorescence microscope. As shown in Fig. 7 (a), on the first day of culture, the cells appeared curled, with most cells not yet spread out and a relatively small number of cells. By the third day, the cell number increased significantly, most cells extended pseudopodia, the nuclei were intact with uniformly distributed chromatin, and the cells were close to each other, while no dead or lysed cells were observed, as shown in Fig. 7 (b). In the above results, differences in cell adhesion number and cytoskeleton morphology between the sterile group and the microbe-containing group indicate that the amount of ion release in the solution affects the biocompatibility of TC4. To directly assess the biosafety of the materials, CCK-8 assays were performed under co-culture conditions. Figure 7 (c) and (d) show the measured OD values and the calculated RGR for the sterile group and the microbe-containing group, respectively. According to ISO 10993-5, a material can be considered non-toxic if the RGR exceeds 75% [38]. In Fig. 7 (d), the RGR values calculated after 1 and 3 days of co-culture were all above 75%, indicating that the samples were non-toxic.

Figure 7 (e, f) shows the release concentrations of Ti, Al, and V ions from samples immersed in *S. mutans*, *V. dispar*, dual-species, and sterile corrosion systems for 7 and 14 days. The results indicate that the dissolved Ti ion concentration in the bacterial-containing groups at day 14 approximately tenfold higher than that at day 7, whereas no significant change was observed in the sterile control. The dissolution of metal ions reflects passive film degradation on the sample surface, leading to accelerated corrosion of TC4. Higher concentrations of metal ions in the solution correspond to more severe corrosion; the dual-species group exhibited the highest corrosion rate.

4. Discussion

Oral biofilms are a complex structure formed by synergistic interactions of various oral bacteria. Multi-species biofilms exhibit characteristics distinct from those of single-species biofilms. To accurately assess bacterial corrosion, this study explored MIC of oral implant material SLM TC4 under a dual-species model of V. dispar and S. mutans. FE-SEM and CLSM results indicated that dual-species biofilms with complex structures readily colonized on the metal surface. Biofilms from different strains differed significantly in composition and adhesion. Electrochemical tests showed the Ti alloy had maximum corrosion current density and minimum charge transfer resistance under dual-species infection. The dual-species biofilm induced pronounced corrosion of the Ti alloy. XPS indicated TiO_2 was partially reduced to Ti_2O_3 and TiO in SLM TC4 passive films, indicating damaged, incomplete passive films, consistent with the correlation between higher metal oxide content and denser passive films [46]. Surface elemental peaks of Ti^0, Al^0, and V^0 were found on dual-species-infected SLM TC4. These results can be attributed to the relatively thinner passive film formed on TC4 in the mixed dual-species medium. Adequate dissolved oxygen is crucial for the formation and repassivation of the passive film on TC4; however, the anaerobic environment within the biofilm on the metal surface inhibits passivation, thereby

reducing the corrosion resistance of the metal specimens. ICP-OES further showed that oral microbiota accelerated the dissolution of Ti, Al, and V ions from SLM TC4. From thermodynamic and kinetic perspectives, systematic investigations have been performed on metal pitting corrosion and ion dissolution [47–49]. The mechanisms of MIC have also been comprehensively reviewed recently [50]. Corrosion increases implant surface roughness, decreases wettability, and impairs mechanical properties, biocompatibility, and implantation stability. The results of in vitro cytotoxicity assays showed that the solutions co-cultured with different bacterial strains exerted differential effects on the stimulation of cell proliferation and adhesion. Elevated concentrations of Ti particles have been detected in dental implants affected by peri-implantitis [51]. Ti particles exhibit cytotoxicity toward peri-implant cells, including osteoblasts, fibroblasts, and lymphocytes [52,53]. Based on this observation, the present study raises a noteworthy concern: metallic materials used in the oral environment may undergo accelerated corrosion due to microbial activity, leading to increased release of metal ions and posing potential carcinogenic risks—a phenomenon that has been largely overlooked in previous research.

Figure 8 shows a schematic of the interdependent growth of S. mutans and V. dispar that jointly promotes biofilm maturation. Microorganisms colonize material surfaces and form biofilms via synergy, eventually establishing stable microbial communities. When coexisting with S. mutans, V. dispar utilizes its metabolic products to enhance its biofilm formation. In turn, V. dispar within the biofilm further promotes the accumulation and formation of S. mutans microcolonies, thereby facilitating mutual growth. SEM and CLSM evidence strongly supports these findings. S. mutans secretes glucosyltransferase B (GtfB), which synthesizes water-soluble (l-glucan) and alkali-soluble glucan polysaccharides [54]. GtfB can be part of the salivary pellicle and adsorb to other oral microbial surfaces. Although *V. dispar* cannot adhere to the acquired pellicle on its own, its cell surface possesses receptors that specifically recognize and bind to the alkali-soluble glucan produced by *S. mutans*. This increases biofilm thickness and structural complexity (Fig. 1) and enhances microbial adhesion and accumulation on dental implant materials [55]. Beyond mediating enhanced adhesion, *Veillonella* species are incapable of catabolizing sugars. They rely on short-chain organic acids derived from the catabolic activities of *S. mutans* as carbon and energy sources, thereby promoting the growth and maturation of *Veillonella* [36]. Moreover, *V. dispar–S. mutans* interaction enhances EPS expression [56]. EPS are critical for biofilm formation and virulence, restricting bidirectional substance diffusion in and out of biofilms. This causes accumulation of acidic compounds capable of dissolving metal ions [57], creating a highly protected and concentrated pathogenic microenvironment within the biofilm. The stable and structurally complex biofilm matrix protects the bacteria from variations in pH, temperature, pressure, mechanical forces, host immune attacks, and antibiotics, thereby enhancing the biofilm's destructive potential.

Ti alloy corrosion in microbial environments is an electrochemical process initiated or accelerated by biofilms. MIC has two main types: EET-MIC and M-MIC [58–60]. EET-MIC features anaerobic respiration and intracellular oxidant reduction, while M-MIC features anaerobic fermentation or respiration with extracellular oxidant reduction [58]. Biofilm formation alters the metal interface microenvironment, resulting in much lower pH beneath the biofilm than in the bulk solution. In acidic environments, the

passive film dissolution forms hydrated oxides, accelerating Ti alloy surface corrosion. *S. mutans* uses sucrose, controlled by GtfB/C and Ftf genes, to produce water-insoluble extracellular polysaccharides; ScrA and ScrB genes regulate sucrose metabolism to produce lactic acid [61]. This creates a low-pH environment under the biofilm, exacerbating microbiologically induced corrosion. In this study, the overall pH of the system even increased after the interaction between *S. mutans* and *V. dispar*. This pH change trend is inconsistent with electrochemical results, indicating metabolic product-induced acid corrosion is not the only mechanism by which *S. mutans–V. dispar* accelerates SLM TC4 corrosion; other mechanisms must exist. We hypothesize that EET-MIC may play a significant role in this process.

Many studies confirm that pathogens with EET ability exist in the human gut [62,63], but research on oral microbial EET remains insufficient. *Veillonella* is identified as an electroactive, corrosive nitrate-reducing bacterium (NRB). Such electroactive microbes and NRBs can transfer electrons extracellularly, potentially causing severe corrosion [64]. Previous research shows nitrate-reducing bacteria can directly take electrons from steel surfaces for energy and metabolism [65]. These processes are enhanced in biofilms because electrons cannot move freely in solution, making their corrosion potential even higher than that of sulfate-reducing bacteria. Adding riboflavin to *V. dispar* inoculated culture medium significantly reduced TC4 samples' charge transfer resistance (R_{ct}) and increased their corrosion rate. This confirms that *Veillonella* uses exogenous riboflavin to boost EET efficiency, thus accelerating microbiologically influenced corrosion. As shown in Fig. 8, reduced riboflavin carries electrons from the TC4 surface to outer-membrane c-type cytochromes (c-Cyts), releases them, and then oxidized riboflavin diffuses back to the metal surface to regain electrons [66]. In this repeated redox cycle within the mixed dual-species biofilm, bacteria use riboflavin to transfer electrons from the metal surface to the cell membrane, driving intracellular biocatalytic nitrate reduction.

5. Conclusions

This study investigated the MIC of SLM TC4 induced by mono- or dual-species biofilms of *V. dispar* and *S. mutans*. Their syntrophic interaction promoted biofilm maturation, structural complexity, and EPS production, causing the most severe pitting on TC4. Furthermore, in the presence of the mixed consortium, the corrosion current density was at least four times higher than that in the abiotic control group, indicating that the microbial community accelerated the release of metal ions. All these results demonstrate that oral microbial communities can accelerate the corrosion rate of TC4. EET-MIC likely played a key role, as exogenous riboflavin enhanced *V. dispar* corrosivity. Using interdisciplinary methods, we established an integrated *in vitro* corrosion-cytotoxicity model to elucidate oral MIC mechanisms. This model predicts long-term clinical performance and biocompatibility of medical metals, guiding material selection for high-risk patients. Given the complex interactions among materials, microbes, and the oral environment, further in-depth research on oral MIC mechanisms is urgently needed.

Declarations

Author Contribution

Y.W. was responsible for writing the original draft, designing the experimental methods, analyzing the experimental results, and reviewing and editing the manuscript.K.Z. was responsible for investigation and validation.Z.L. was responsible for validation and project administration.H.Y. Yuan was responsible for providing resources and supervising the research.X. F. and X. Z. were responsible for formal analysis, resources, reviewing and editing, and supervision.

Acknowledgements

This work was supported by the National Natural Science Foundation of China (No. 52301091), Medical and Health Science and Technology Project of Zhejiang Province (2024KY024).

Data Availability

All data supporting the findings of this study are available within the paper and its Supplementary Information.

References

1. Aoyagi, H., Okada, M., Yanagimoto, H. & Matsumoto, T. Investigation on bacterial capture and antibacterial properties of acid-treated Ti surface. *Dental Materials* 40, 318–326 (2024).
2. Zhou, X. *et al.* Cu alloying enabling dual biocorrosion suppression and fatigue crack mitigation in SLM-processed titanium implants with retained osteogenic activity. *Journal of Materials Science & Technology* 247, 95–108 (2026).
3. Davoodi, E. *et al.* Additively manufactured metallic biomaterials. *Bioactive Materials* 15, 214–249 (2022).
4. Tomova, Z., Chonin, A., Stoeva, I. & Vlahova, A. Clinical and laboratory study of corrosion resistance of a base dental alloy for selective laser melting. *Folia Medica* 65, 664–670 (2023).
5. Moghanian, A. *et al.* New trends in 3D and 4D printed dental and orthopedic Implants: Methods, applications and future directions. *Bioprinting* 48, e00406 (2025).
6. Rattner, N. *et al.* 3D-Printed Titanium Implants with Bioactive Peptide-Polysaccharide Scaffolds for Personalized Bone Reconstruction. *Advanced healthcare materials*, e05131 (2026).
7. Liu, X., Ishak, M. I., Ma, H., Su, B. & Nobbs, A. H. Bacterial Surface Appendages Modulate the Antimicrobial Activity Induced by Nanoflake Surfaces on Titanium. *Small* 20, 2310149 (2024).
8. Joshi, A. A. *et al.* Integrative microbiome- and metatranscriptome-based analyses reveal diagnostic biomarkers for peri-implantitis. *npj Biofilms and Microbiomes* 11, 175 (2025).

9. Guglielmotti, M. B., Olmedo, D. G. & Cabrini, R. L. Research on implants and osseointegration. *Periodontol* 2000, 79 (2019).
10. Wang, Q. *et al.* Oral microbiota accelerates corrosion of 316L stainless steel for orthodontic applications. *Journal of Materials Science & Technology* 128, 118–132 (2022).
11. Niu, Q. *et al.* Dynamics of the oral microbiome during orthodontic treatment and antimicrobial advances for orthodontic appliances. *iScience* 27, 111458 (2024).
12. Qian, H., Wang, T., Zhang, B. & Meng, G. The acceleration of localized copper corrosion by extracellular polymeric substances of sulfate-reducing bacteria. *Bioelectrochemistry* 165, 108980 (2025).
13. Souza, J. G. S. *et al.* Titanium particles and ions favor dysbiosis in oral biofilms. *Journal of Periodontal Research* 55, 258–266 (2020).
14. Qi, P., Zeng, Y., Zhang, D., Sun, Y. & Wang, P. The biofilm-metal interface: A hotspot for microbiologically influenced corrosion. *Cell Reports Physical Science* 6, 102500 (2025).
15. Aslan, C., Baihaqi, B., Devianto, H., Wonoputri, V. & Harimawan, A. Microbiologically influenced corrosion in petrodiesel-biodiesel storage system: A review. *Biomass and Bioenergy* 201, 108075 (2025).
16. Okoro, C. C. *et al.* Analysis of microbial communities associated with corrosion in low Sulphate/saline oil bearing environment. *Science of The Total Environment* 986, 179737 (2025).
17. Yu, S., Lu, X. & Lu, H. Marine microbial biofilms on diverse abiotic surfaces. *Frontiers in Marine Science* 12 (2025).
18. Ma, Y. *et al.* Microbiologically influenced corrosion of marine steels within the interaction between steel and biofilms: a brief view. *Applied Microbiology and Biotechnology* 104, 515–525 (2020).
19. Gu, T., Jia, R., Unsal, T. & Xu, D. Toward a better understanding of microbiologically influenced corrosion caused by sulfate reducing bacteria. *Journal of Materials Science & Technology* 35, 631–636 (2019).
20. Liu, X., Fan, Y., Wang, F. & Xu, D. Riboflavin-mediated extracellular electron transfer enhances microbiologically influenced corrosion of 316L stainless steel by Listeria monocytogenes. *npj Materials Degradation* 9, 139 (2025).
21. Zeng, F. *et al.* Adsorption of Candida albicans on Ti-6Al-4V surface and its corrosion effects in artificial saliva. *Bioelectrochemistry* 148, 108248 (2022).
22. Jiang, C. *et al.* Cariogenic Streptococcus mutans accelerates the crevice corrosion of 316L stainless steel in simulated oral environment. *Bioelectrochemistry* 170, 109227 (2026).
23. Gopalakrishnan, U. *et al.* Assessing the Potential Association Between Microbes and Corrosion of Intra-Oral Metallic Alloy-Based Dental Appliances Through a Systematic Review of the Literature. *Frontiers in Bioengineering And Biotechnology* 9 (2021).
24. Yang, C. *et al.* Corrosion behavior of high nitrogen nickel-free austenitic stainless steel in the presence of artificial saliva and Streptococcus mutans. *Bioelectrochemistry* 142, 107940 (2021).

25. Yang, Y. *et al.* Streptococcus mutans biofilms induce metabolite-mediated corrosion of 316 L stainless steel in a simulated oral environment. *Corrosion Science* 182, 109286 (2021).
26. Yu, S. *et al.* Pyruvate metabolism is involved in adaptability and cariogenicity of Streptococcus mutans. *Journal of oral microbiology* 18, 2612843 (2026).
27. Zheng, T. *et al.* Regulatory mechanisms of exopolysaccharide synthesis and biofilm formation in Streptococcus mutans. *Journal of oral microbiology* 15 (2023).
28. Wu, J. *et al.* Influence of Candida albicans-Streptococcus mutans cross-border interactions on the corrosion behaviour of Ti and Ti-Zr in artificial saliva. *Corrosion Science* 233, 112101 (2024).
29. Alonso-Español, A. *et al.* Antimicrobial Effect and Cytocompatibility After Using Different Decontamination Methods on Titanium Implant Surfaces: An In Vitro Study. *Clinical oral implants research* 36, 626–639 (2025).
30. Villegas, M. *et al.* Emerging Strategies to Prevent Bacterial Infections on Titanium-Based Implants. *Small* 20, 2404351 (2024).
31. Mashima, I. & Nakazawa, F. The influence of oral Veillonella species on biofilms formed by Streptococcus species. *Anaerobe* 28, 54–61 (2014).
32. Do, T., Sheehy, E. C., Mulli, T., Hughes, F. & Beighton, D. Transcriptomic analysis of three Veillonella spp. present in carious dentine and in the saliva of caries-free individuals. *Frontiers in cellular and infection microbiology* 5, 25 (2015).
33. Mashima, I. & Nakazawa, F. The interaction between Streptococcus spp. and Veillonella tobetsuensis in the early stages of oral biofilm formation. *Journal of Bacteriology* 13 197 (2015).
34. Leo, J. C. Interaction between bacterial adhesins leads to coaggregation by the oral bacteria Veillonella parvula and Streptococcus gordonii. *MBIO* 16 (2025).
35. Dorison, L. *et al.* Identification of Veillonella parvula and Streptococcus gordonii adhesins mediating co-aggregation and its impact on physiology and mixed biofilm structure. *MBIO* 15 (2024).
36. Luo, Y. X. *et al.* Research progress in the relationship between Veillonella and oral diseases. *West China journal of stomatology* 38, 576–582 (2020).
37. Liu, S. *et al.* Effect of Veillonella parvula on the physiological activity of Streptococcus mutans. *Archives of oral biology* 109, 104578 (2020).
38. Zhou, X. *et al.* Microstructural evolution, corrosion behavior and cytotoxicity of Ti-6Al-4V/ZrO2 composite fabricated by directed energy deposition for implant biomaterial. *Journal of Alloys and Compounds* 892, 161820 (2022).
39. Li, J.-H. *et al.* Chloride-dependent enhancement of microbiologically influenced corrosion on X80 steel by Desulfovibrio desulfuricans: the critical role of extracellular polymeric substances. *Petroleum Science* 23, 4 (2025).
40. Zhou, E. *et al.* Accelerated biocorrosion of stainless steel in marine water via extracellular electron transfer encoding gene phzH of Pseudomonas aeruginosa. *Water Research* 220, 118634 (2022).

41. Jin, Y. *et al.* Electrically conductive nanowires controlled one pivotal route in energy harvest and microbial corrosion via direct metal-microbe electron transfer. *Journal of Materials Science & Technology* 174, 226–233 (2024).
42. Liu, X., Zhou, E., Fan, Y., Wang, F. & Xu, D. Riboflavin-mediated extracellular electron transfer enhances microbiologically influenced corrosion of 316L stainless steel by Enterococcus faecalis. *Bioelectrochemistry* 165, 108982 (2025).
43. Zha, L., Li, H. & Wang, N. In Situ Electrochemical Study of the Growth Kinetics of Passive Film on TC11 Alloy in Sulfate Solution at 300°C/10 MPa. *Materials* 13, 5 (2020).
44. Yao, K. *et al.* Photoelectron Therapy Preventing the Formation of Bacterial Biofilm on Titanium Implants. *Small* 21, 2409824 (2025).
45. Wang, Y., Yu, Z., Li, K. & Hu, J. Effects of surface properties of titanium alloys modified by grinding, sandblasting and acidizing and nanosecond laser on cell proliferation and cytoskeleton. *Applied Surface Science* 501, 144279 (2020).
46. Kotsakis, G. A. *et al.* Dynamic assessment of titanium surface oxides following mechanical damage reveals only partial passivation under inflammatory conditions. *npj Materials Degradation* 8, 98 (2024).
47. Li, Q. *et al.* Kinetics of the hydrogen absorption and desorption processes of hydrogen storage alloys: A review. *International Journal of Minerals, Metallurgy and Materials* 29, 32–48 (2022).
48. Li, Q., Peng, X. & Pan, F. Magnesium-Based Materials for Energy Conversion and Storage. *Journal of Magnesium and Alloys* 9, 2223–2224 (2021).
49. Li, Q. *et al.* Thermodynamics and kinetics of hydriding and dehydriding reactions in Mg-based hydrogen storage materials. *Journal of Magnesium and Alloys* 9, 1922–1941 (2021).
50. Lekbach, Y. *et al.* Microbial corrosion of metals: The corrosion microbiome. *Advances in Microbial Physiology* 78, 317–390 (2021).
51. Lorenzi, S. *et al.* A comparative study on the corrosion resistance of Ti-6Al-4V produced via material extrusion and other additive manufacturing technologies. *npj Materials Degradation* 10, 32 (2026).
52. Vegas-Bustamante, E. *et al.* Cytocompatibility and Microbiological Effects of Ti6Al4V Particles Generated During Implantoplasty on Human Fibroblasts, Osteoblasts, and Multispecies Oral Biofilm. *Materials* 18, 24 (2025).
53. Kotsakis, G. A. *et al.* Effect of implant cleaning on titanium particle dissolution and cytocompatibility. *J Periodontol* 92, 580–591 (2021).
54. Zhang, Q., Ma, Q., Wang, Y., Wu, H. & Zou, J. J. I. J. o. O. S. Molecular mechanisms of inhibiting glucosyltransferases for biofilm formation in Streptococcus mutans. <background-color:#CCFF99;ivertical-align:super;display:none;>Int J Oral Sci</background-color:#CCFF99;ivertical-align:super;display:none;><vertical-align:sub;> </vertical-align:sub;>13, 30 (2021).
55. Dorison, L. *et al.* Identification of V. parvula and S. gordonii adhesins mediating co-aggregation and its impact on physiology and mixed biofilm structure. *mBio* 15, 12 (2024).

56. Li, G. *et al.* Veillonella parvula promotes root caries development through interactions with Streptococcus mutans and Candida albicans. *MICROBIAL BIOTECHNOLOGY* 17, (2024).
57. Naveed, S. *et al.* Microalgal extracellular polymeric substances and their interactions with metal (loid) s: A review. *Technology* 49, 1769–1802 (2019).
58. Li, Y. *et al.* Anaerobic microbiologically influenced corrosion mechanisms interpreted using bioenergetics and bioelectrochemistry: a review. *Technology* 34, 1713–1718 (2018).
59. Gu, T., Wang, D., Lekbach, Y. & Xu, D. J. C. O. i. E. Extracellular electron transfer in microbial. *Biocorrosion* 29, 100763 (2021).
60. Su, Z., Chao, Z., Jiang, V., Daniel, S. & Banta, S. Site Directed Mutagenesis of the Cyc2 Outer Membrane Protein from Acidithiobacillus ferrooxidans Reveals a Critical Role for Bound Iron Atoms in Extracellular Electron Transfer. *Small* 21, 2408837 (2025).
61. de Lucena, F. S. *et al.* Drug repurposing for glucosyltransferase inhibition for targeted oral biofilm disruption. *NPJ Biofilms Microbiomes* 56, (2026).
62. Naradasu, D., Miran, W., Sakamoto, M. & Okamoto, A. J. F. i. m. Isolation and characterization of human gut bacteria capable of extracellular electron transport by electrochemical. *techniques* 9, 3267 (2019).
63. Wang, W. *et al.* Bacterial extracellular electron transfer occurs in mammalian gut. *Analytical Chemistry* 91, 12138–12141 (2019).
64. Mohd Zaidi, M. A. F., Masri, M. N. & Kew, W. S. Microbiologically influenced corrosion of iron by nitrate reducing Bacillus sp. *Journal of Physics: Conference Series* 12, 12–66 (2021)
65. Zhou, E. *et al.* Direct microbial electron uptake as a mechanism for stainless steel corrosion in aerobic. *environments* 219, 118553 (2022).
66. Xu, Z. *et al.* Accelerated development of Ti-6Al-4V microbial corrosion triggered by electroactive sulfate-reducing Desulfovibrio ferrophilus biofilm in enriched artificial seawater containing soluble. *electron shuttle* 220, 111306 (2023).

Figures

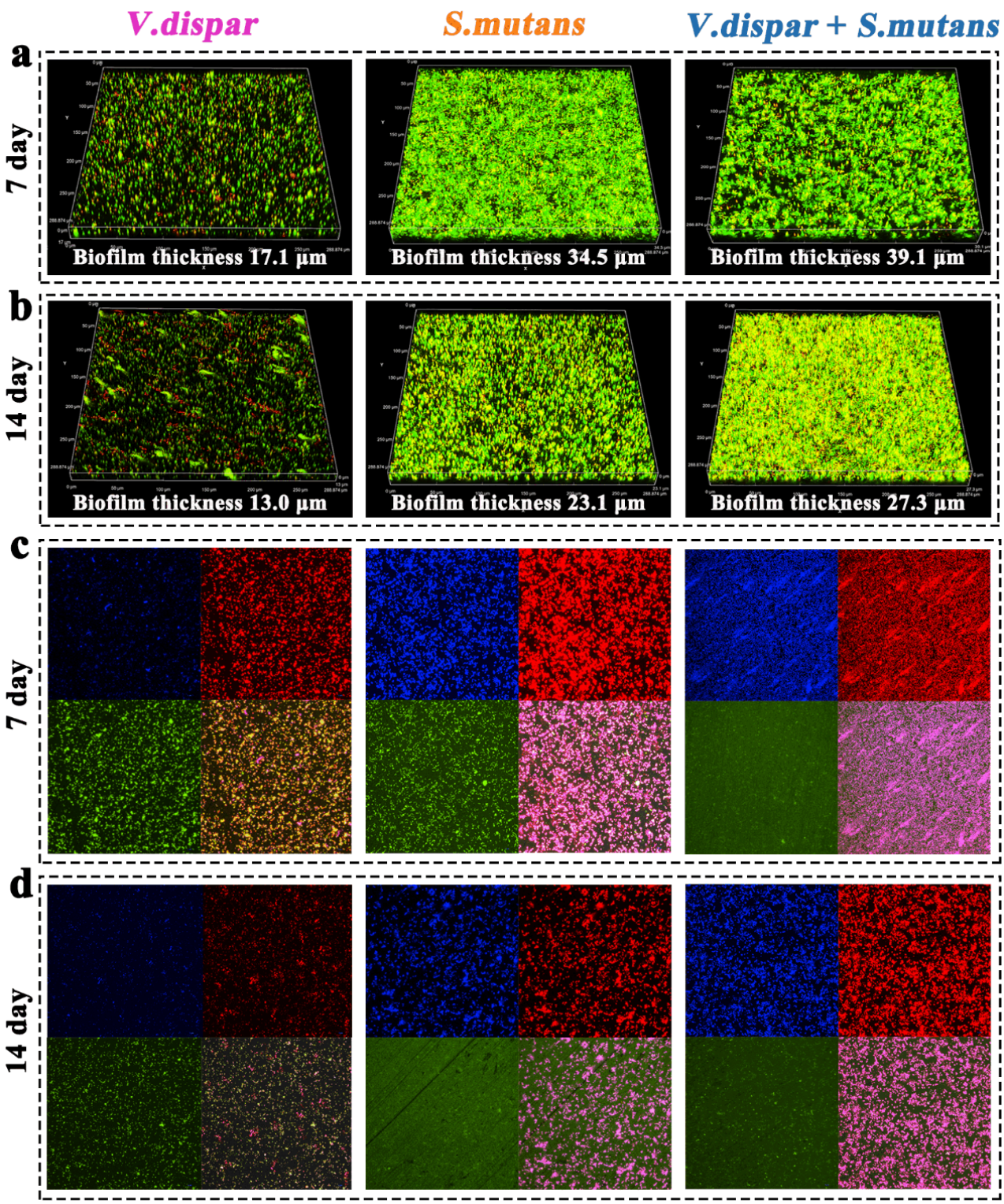

Figure 1

3D CLSM images of different biofilms after 7 days (a, c) and 14 days (b, d) of cultivation. Panels (a, b) show CLSM images of biofilms stained with live/dead viability dye. Panels (c, d) display merged images depicting cells (blue), proteins (red), and polysaccharides (green). The biofilms correspond to *S. mutans*, *V. dispar*, and the mixed consortium of *S. mutans* and *V. dispar*.

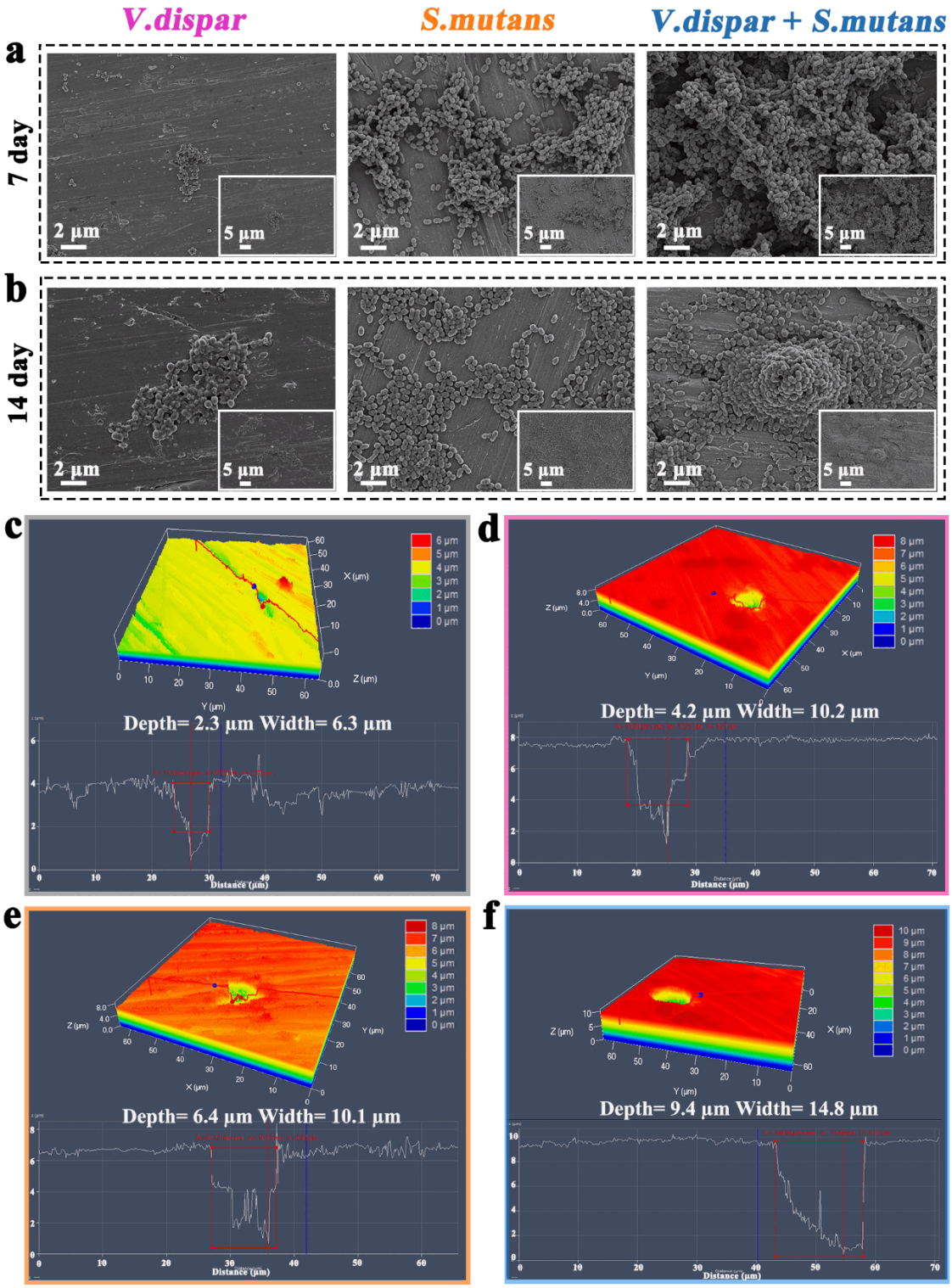

Figure 2

SEM images of TC4 coupons after immersion in the culture media of *V. dispar*, *S. mutans*, and the microbial mixture of *V. dispar* and *S. mutans* for 7 days (a) and 14 days (b). CLSM images of pits on the TC4 surface after removal of biofilms and corrosion products following 14 days of immersion: (c) sterile culture medium, (d) *V. dispar* culture medium, (e) *S. mutans*culture medium, (f) mixed microbial culture medium.

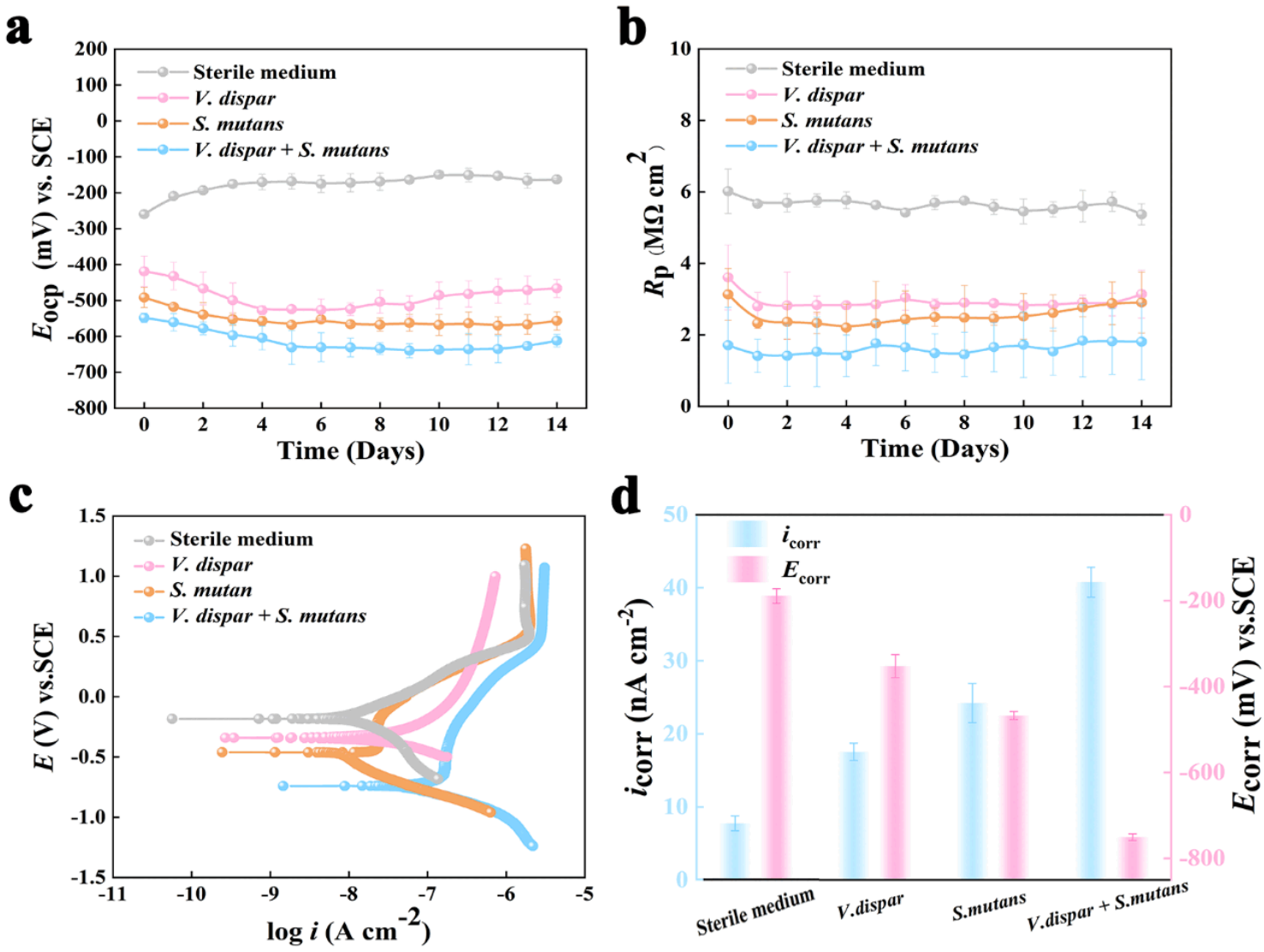

Figure 3

Electrochemical analyses of TC4 coupons after immersion in different media for 14 days: (a) open circuit potential over time; (b) polarization resistance over time; (c) potentiodynamic polarization curves of TC4 after exposure to different media; (d) fitted corrosion parameters obtained from potentiodynamic polarization curves.

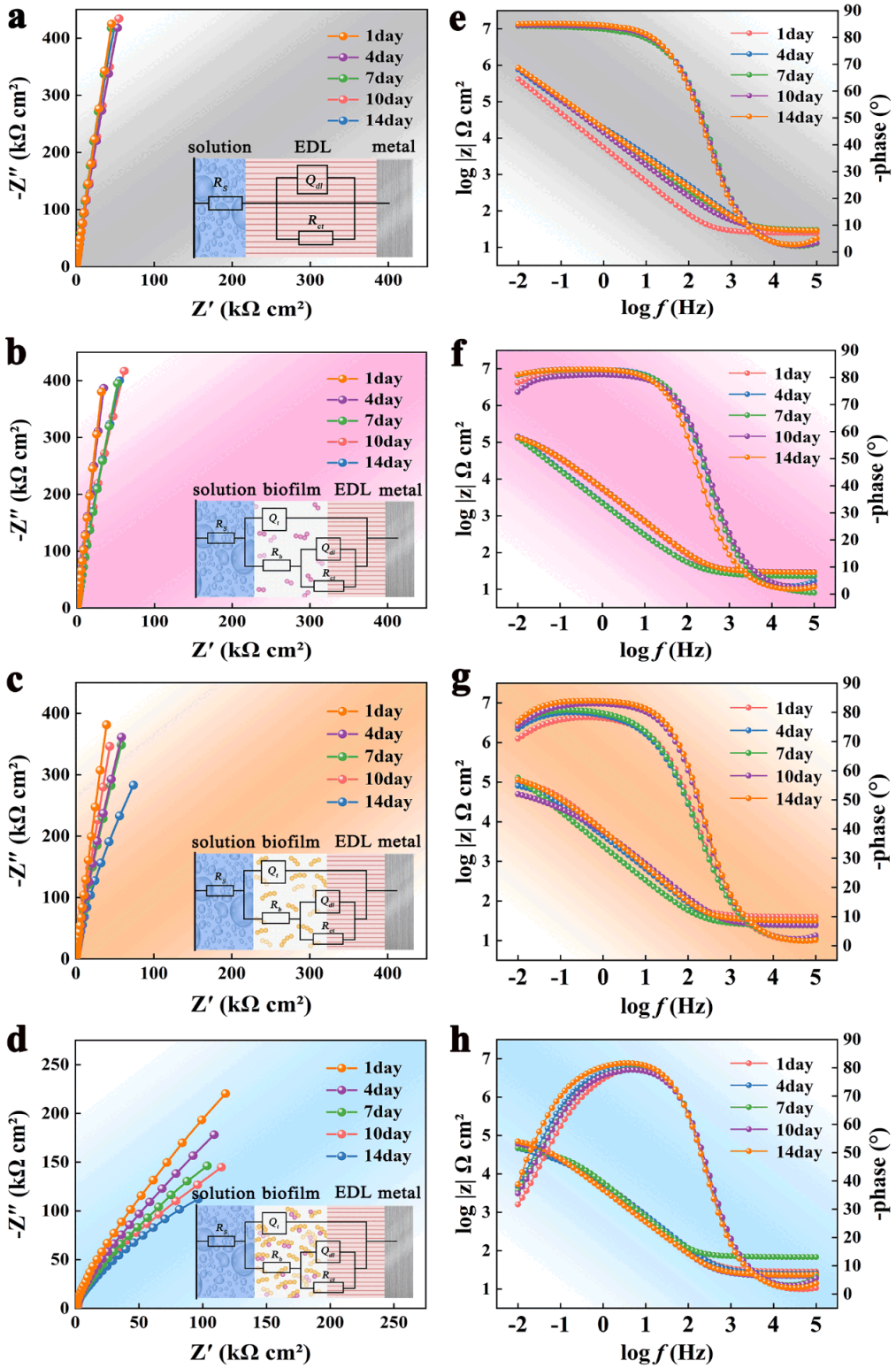

Figure 4

Variations of Nyquist (a-d) and Bode plots (e-h) of the coupons exposed to different culture media for different times: (a, e) abiotic medium, (b, f) *V. dispar*, (c, g) *S.mutans*, and (d, h) the microbial mixture of *V. dispar* and *S.mutans*

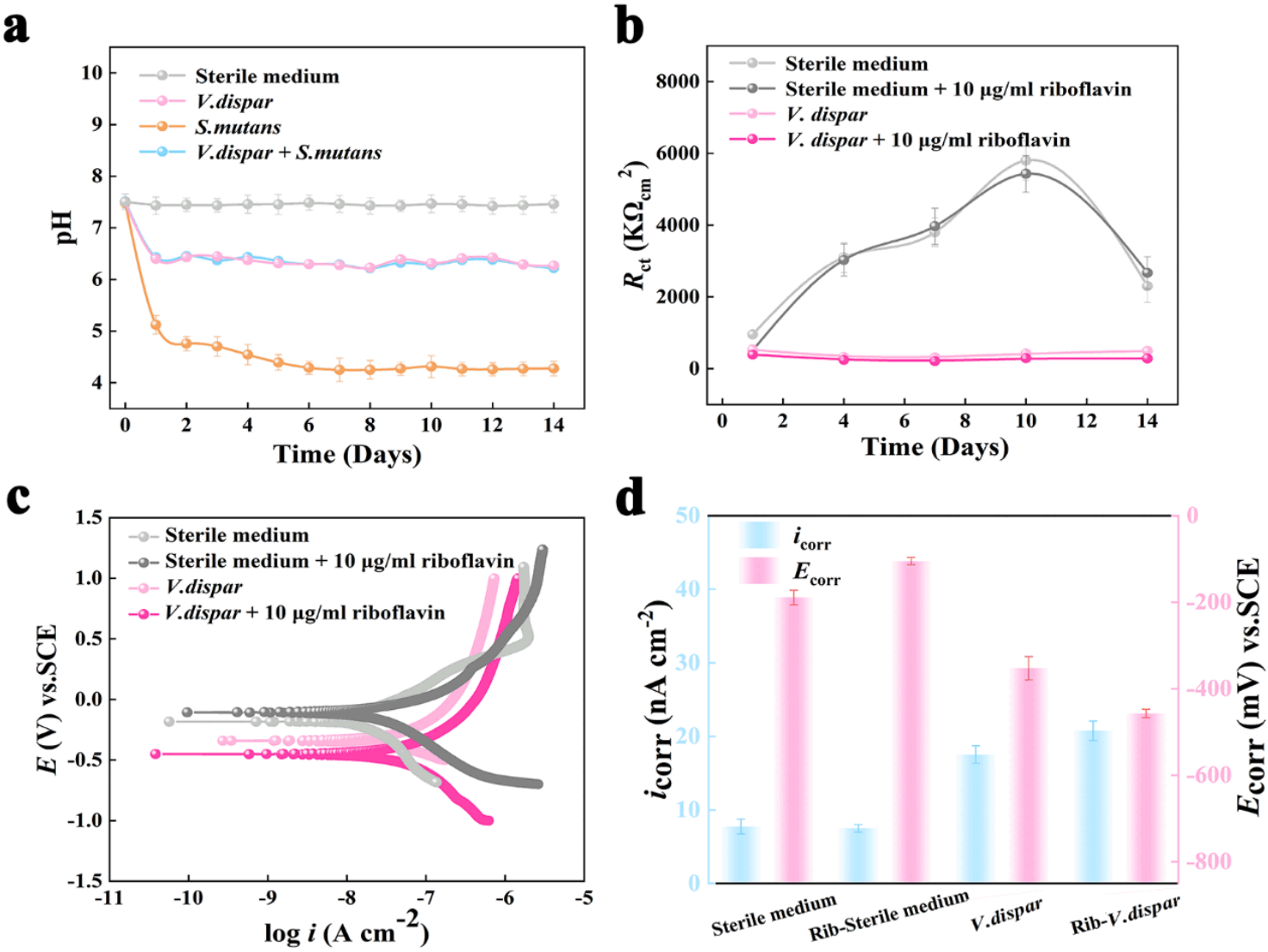

Figure 5

Variations in pH values of TC4 specimens during 14-day exposure to *S. mutans*, *V. dispar*, and their dual-species co-culture are shown(a). Electrochemical analyses of TC4 coupons after 14 days of immersion in abiotic and *V. dispar*-inoculated media with and without the addition of riboflavin: (b) Time-dependent variation of charge transfer resistance (R_{ct}) obtained from fitted EIS data; (c) Potentiodynamic polarization curves of TC4 after exposure to different media; (d) Fitted corrosion parameters obtained from potentiodynamic polarization curves.

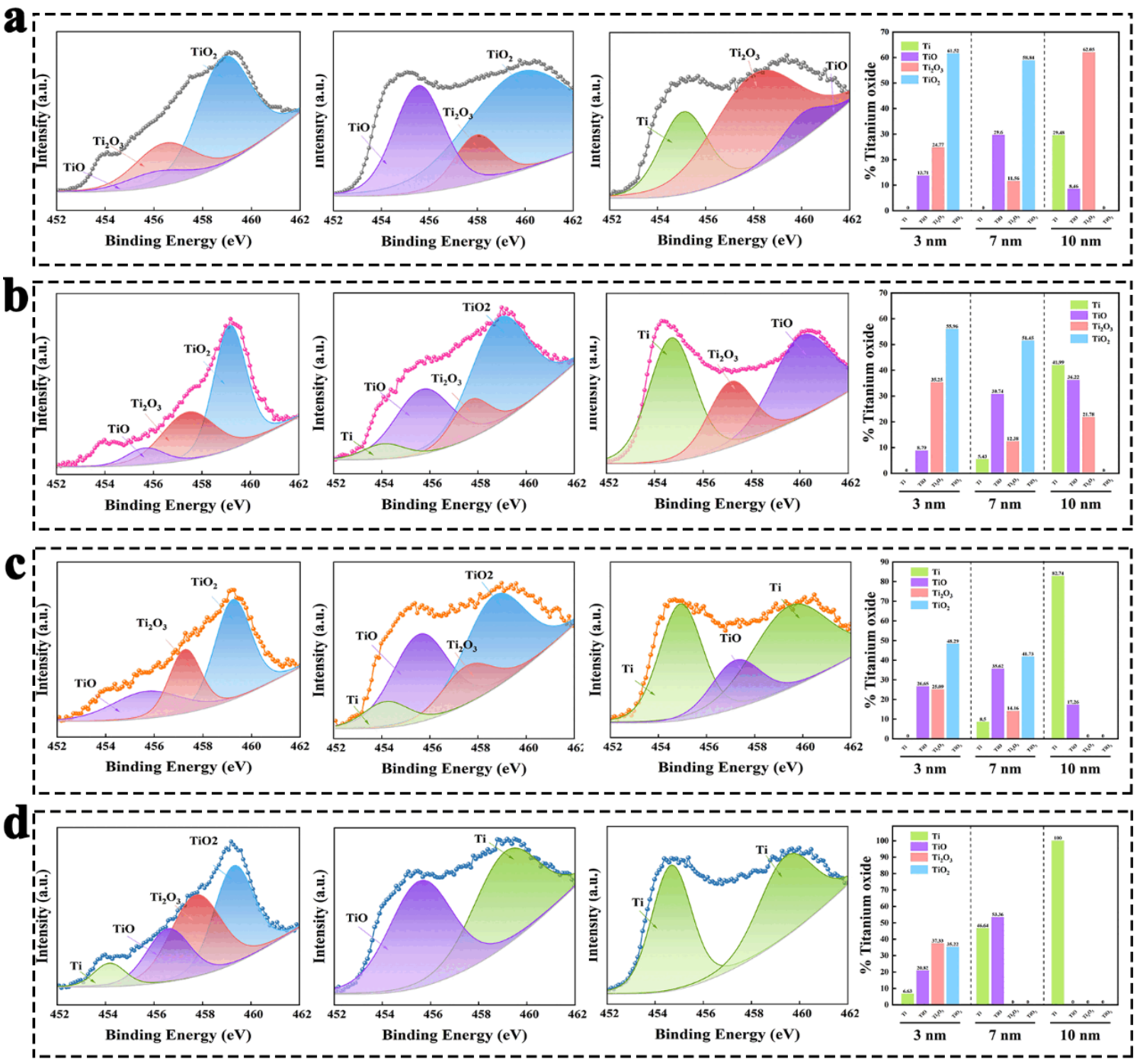

Figure 6

Detailed high-resolution XPS spectra of Ti 2p at depths of 3 nm, 7 nm, and 10 nm for TC4 after 14 days of immersion under different culture conditions, and the cation percentages of Ti 2p peaks: (a) Sterile medium, (b) *V. dispar*, (c) *S. mutans*, and (d) microbial consortium of *V. dispar* and *S. mutans*.

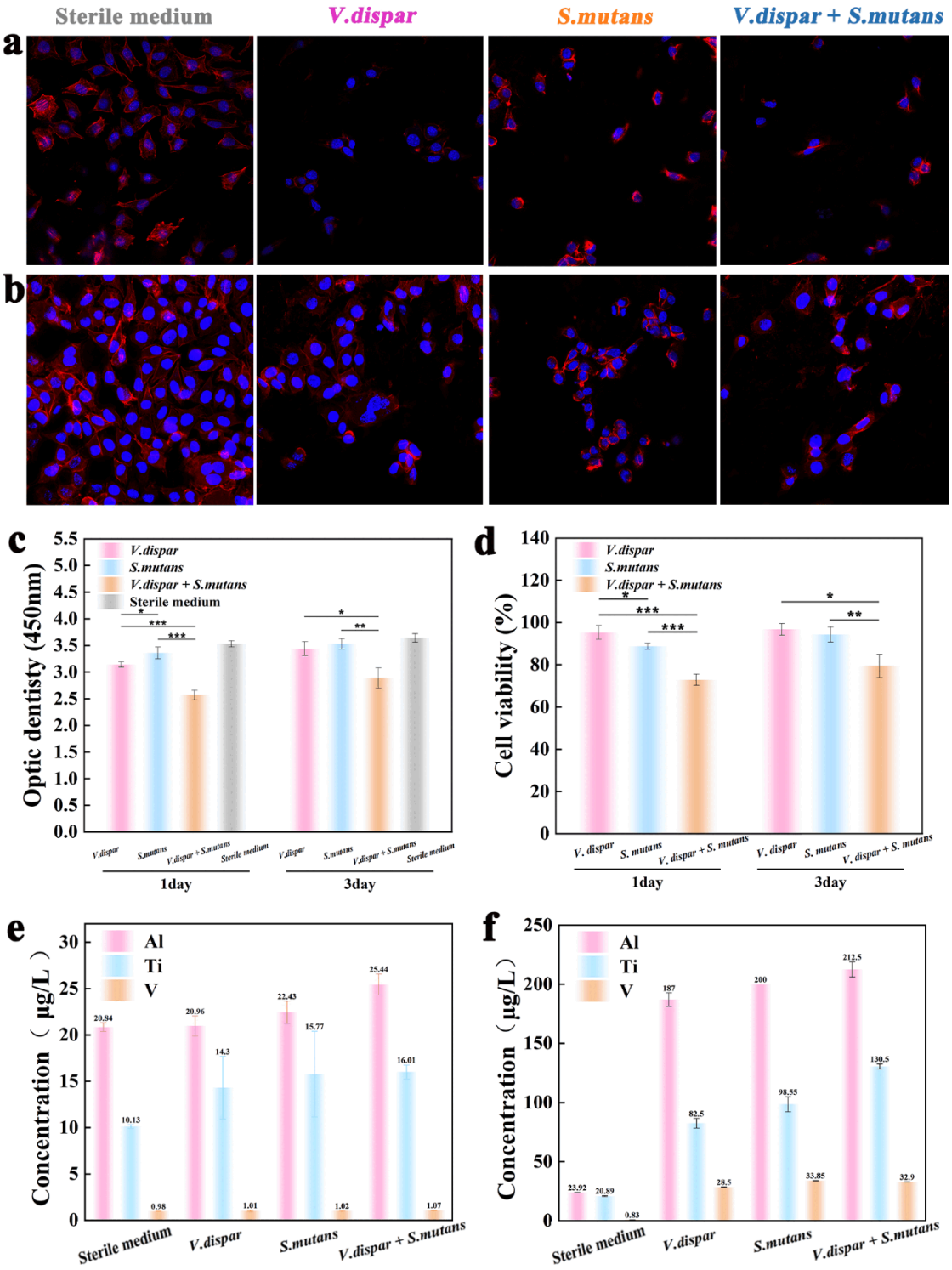

Figure 7

After 1 (a) and 3 days (b) of co-culture, the cytoskeleton staining results of the sterile group and the microbe-containing group, as well as the cytotoxicity of the sterile group and the microbe-containing group (c, d); the dissolution of Ti, Al, and V ions from TC4 samples after 7 days (e) and 14 days (f) of immersion.

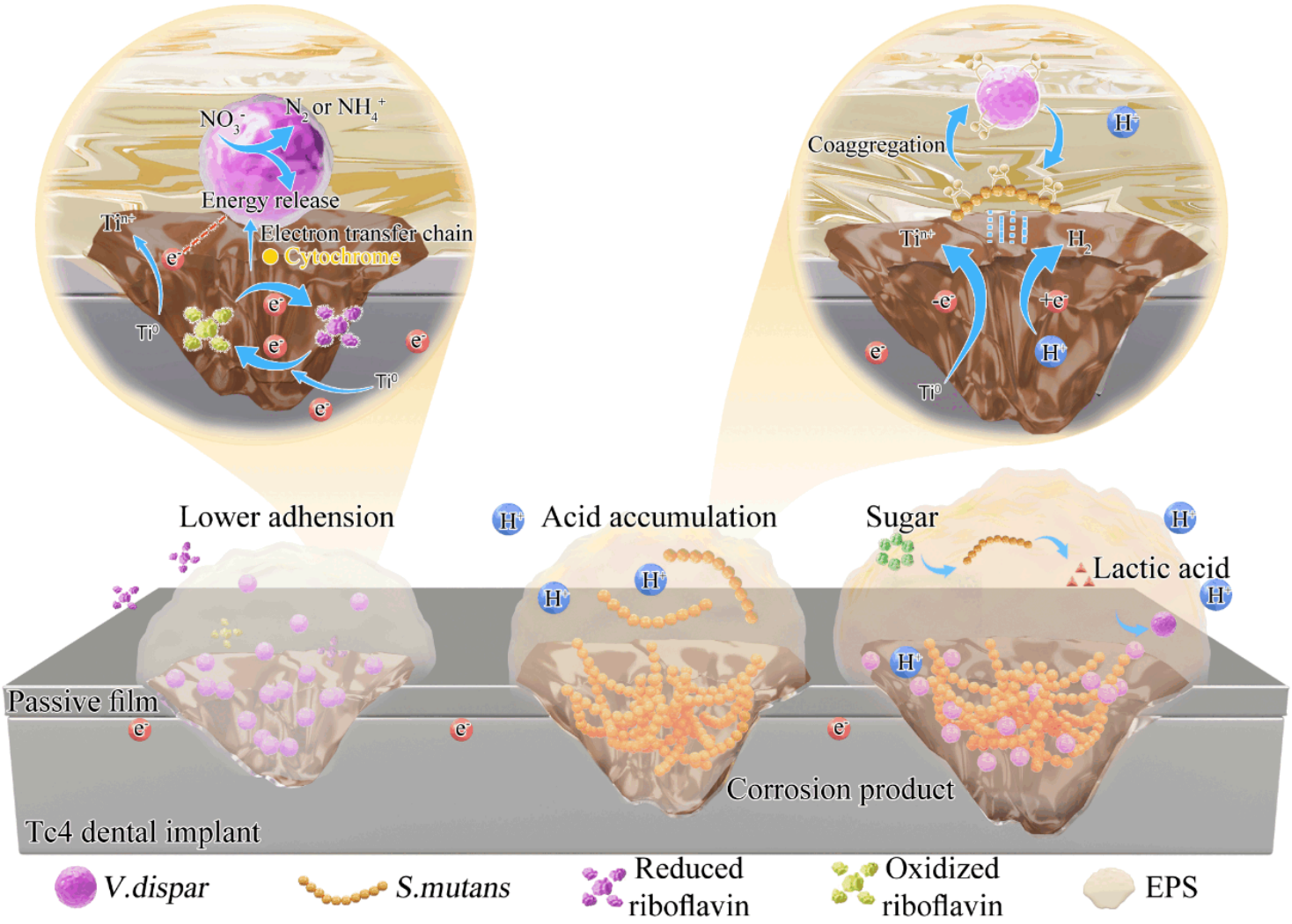

Figure 8

Illustration of the MIC mechanism in the microbial mixture of *V. dispar* and *S. mutans*.